nature materials

Article

https://doi.org/10.1038/s41563-023-01740-9

Solution-processable mixed-anion cluster chalcohalide $Rb_6Re_6S_8I_8$ in a light-emitting diode

Received: 12 February 2023

Accepted: 24 October 2023

Published online: 3 January 2024

Check for updates

Craig C. Laing[1], **Daehan Kim**[1], **Jinu Park**[2], **Jiahong Shen**[3], **Ido Hadar**[1], **Justin M. Hoffman**[1,5], **Jiangang He**[3], **Byungha Shin**[2], **Chris Wolverton**[3] & **Mercouri G. Kanatzidis**[1,4] ✉

Rhenium chalcohalide cluster compounds are a photoluminescent family of mixed-anion chalcohalide cluster materials. Here we report the new material $Rb_6Re_6S_8I_8$, which crystallizes in the cubic space group $Fm\bar{3}m$ and contains isolated $[Re_6S_8I_6]^{4-}$ clusters. $Rb_6Re_6S_8I_8$ has a band gap of 2.06(5) eV and an ionization energy of 5.51(3) eV, and exhibits broad photoluminescence (PL) ranging from 1.01 eV to 2.12 eV. The room-temperature PL exhibits a PL quantum yield of 42.7% and a PL lifetime of 77 µs (99 µs at 77 K). $Rb_6Re_6S_8I_8$ is found to be soluble in multiple polar solvents including *N*,*N*-dimethylformamide, which enables solution processing of the material into films with thickness under 150 nm. Light-emitting diodes based on films of $Rb_6Re_6S_8I_8$ were fabricated, demonstrating the potential for this family of materials in optoelectronic devices.

Discovery of optically active materials is crucial for developing improved optoelectronic devices such as solar cells[1–3] and light-emitting diodes (LEDs)[4,5]. Extensive research has focused on traditional and novel hybrid perovskite materials due to their exceptional properties, such as intense photoluminescence (PL) and ease of processing into thin films, enabling cost-effective device integration. Chalcohalides, a class of mixed anion materials, have garnered interest for nonlinear optics and energy due to their optical properties and thermal and chemical stability[6–9]. Rhenium chalcohalides, a subcategory based on hexanuclear rhenium (III) clusters, exhibit broad PL in the red-to-near-infrared region[10–13]. The initial discovery of $Re_6Se_4Cl_{10}$ and $Re_6Q_4Br_{10}$ (Q = Se, Te)[14,15] paved the way for soluble phases $KRe_6Se_5Cl_9$ and later $Cs_5Re_6S_8Cl_7$, which contain isolated $[Re_6S_8X_6]^{4-}$ (X = Cl, Br, I) clusters, bridging the gap between solid-state and solution-phase chemistry[16–18]. Further studies incorporated them into polymers and extended-framework materials[19–21], created derivative hybrid organic-cluster compounds and investigated their potential use in catalysis[22,23], as therapeutic antitumoral agents[24] and as functional two-dimensional (2D) semiconductors[25–28]. Gabriel et al.[29] further discuss their chemistry and properties.

The solubility of many rhenium chalcohalide phases also allows for solution-processed thin films, demonstrated in this work, which in combination with their PL makes them a promising class of materials for optoelectronic applications. This solubility is achieved by controlling their structure, bonding and dimensionality through stepwise dimensional reduction. The parent structure is the $Re_6S_8Cl_2$ structure type, shared by $Re_6Q_8X_2$ (Q = S, Se; X = Br, I)[13,30–32], while $Re_6Se_8Cl_2$ adopts a different 2D layered structure[33]. The cluster core consists of six rhenium atoms forming an octahedral arrangement, with one chalcogen atom bonded to each face of the octahedra. In the three-dimensional structure, intercluster bonds connect the cores through either a bridging Re−X−Re bond or a pair of Re−Q bonds. By introducing an alkali metal halide (AX) salt with a sufficiently large A cation[13], the intercluster bonds are broken. The alkali metal fills voids and maintains charge balance, while the halide disrupts intercluster bonds, starting with the bridging Re−X−Re bonds and progressing to the

---

[1] Department of Chemistry, Northwestern University, Evanston, IL, USA. [2] Department of Materials Science and Engineering, Korea Advanced Institute of Science and Technology, Daejeon, Republic of Korea. [3] Department of Materials Science and Engineering, Northwestern University, Evanston, IL, USA. [4] Materials Science Division, Argonne National Laboratory, Lemont, IL, USA. [5] Present address: X-Ray Science Division, Argonne National Laboratory, Lemont, IL, USA. ✉e-mail: m-kanatzidis@northwestern.edu

Re–Q bonds. The Cs/Re/S/Br system highlights how this controlled process results in materials with various dimensionalities such as three-dimensional $Re_6S_8Br_2$[30], 2D $CsRe_6S_8Br_3$[34] with $[Re_6S_8Br_3]^-$ layers, one-dimensional $Cs_2Re_6S_8Br_4$[35] with $[Re_6S_8Br_4]^{2-}$ infinite polymeric chains, and zero-dimensional (0D) $Cs_4Re_6S_8Br_6$[35]. The 0D structure, consisting of Cs^+ ions and isolated $[Re_6Q_8X_6]^{4-}$ (X = Cl, Br, I)[30] clusters, enables solubility in polar solvents such as *N*,*N*-dimethylformamide (DMF)[17,36,37].

This work explores $Rb_6Re_6S_8I_8$, a new fully inorganic rhenium chalcohalide, highlighting its structural, thermal, optical and electronic properties. $Rb_6Re_6S_8I_8$ exhibits broad room-temperature (RT) PL ranging from 1.01 eV to 2.12 eV (1,230 nm to 585 nm) with a remarkable photoluminescence quantum yield (PLQY) of 42.7% and PL lifetime of 77 μs. Thin films of $Rb_6Re_6S_8I_8$ are easily fabricated through a one-step solution-based spin-coating method, enabling their incorporation as the active layer in a rhenium chalcohalide cluster-based LED device.

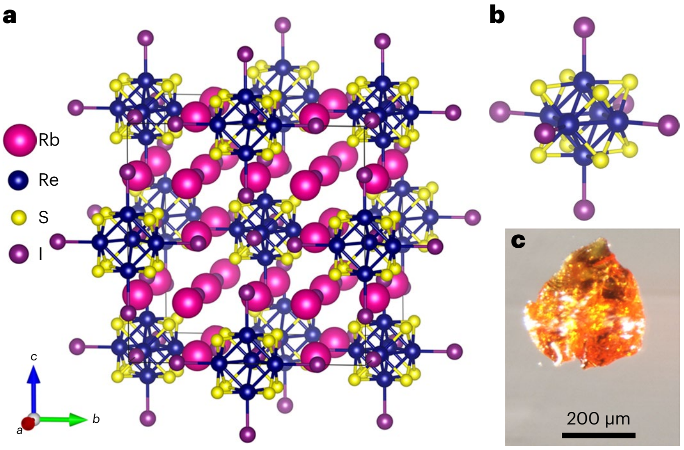

Fig. 1 | $Rb_6Re_6S_8I_8$ crystal structure. a, Crystal structure of $Rb_6Re_6S_8I_8$. **b**, Isolated $[Re_6S_8I_6]^{4-}$ cluster. **c**, $Rb_6Re_6S_8I_8$ single crystal.

Synthesis and thermal characterization

$Rb_6Re_6S_8I_8$ crystals were grown using a RbI salt flux and excess I_2 and then mechanically separated. The stoichiometric ratio of RbI:Re:S:I_2 (20:6:8:4) was heated to 800 °C in a sealed tube under vacuum. Upon heating, the RbI melts, allowing some gaseous iodine to dissolve via $I_2 + I^- \rightarrow I_3^-$. The dissolved iodine then reacts with Re and S, forming clusters and eventually crystallizing upon cooling into $Rb_6Re_6S_8I_8$. Proper preparation requires control of the iodine pressure and temperature gradient for the reaction vessel. Managing the amount of iodine and the reaction vessel volume can ensure that excess iodine pressure does not explode the reaction vessel, while positioning the starting material at the cooler end of the tube furnace with the opposite end of the tube positioned in the hotter centre suppresses chemical vapour transport of ReS_2 away from the RbI flux.

Larger quantities of $Rb_6Re_6S_8I_8$ were prepared by reacting RbI as a limiting reagent followed by recrystallization for purification. The stoichiometric ratio of RbI:Re:ReS_2:I_2 (4:2:4:4.5) was heated in a sealed tube under vacuum to 850 °C for 4 d. The mixture was then ground, homogenized and sealed in a new tube with additional iodine, and heated again to 850 °C for 4 d. Powder X-ray diffraction (PXRD) analysis confirmed the absence of RbI reflections (Supplementary Fig. 1). After grinding and dissolving in DMF, the concentrated solution was syringe filtered and recrystallized by heating at 110 °C overnight. Detailed experimental procedures are available in Supplementary Information along with images (Supplementary Fig. 2).

Differential thermal analysis was carried out using $Rb_6Re_6S_8I_8$ sealed in an ampoule under vacuum (Supplementary Fig. 3a) by cycling from RT to 850 °C twice. Reproducible melting and crystallization events were observed at 757 °C and 745 °C. PXRD analysis (Supplementary Fig. 3b) reveals that $Rb_6Re_6S_8I_8$ is recovered as the primary phase, with a small ReS_2 reflection present. Additionally, residual I_2 was observed at the top of the ampoule after the differential thermal analysis and the previously orange crystals (Fig. 1c) had darkened in colour, indicating that a small degree of decomposition occurs when $Rb_6Re_6S_8I_8$ is melted under vacuum.

Crystal structure

$Rb_6Re_6S_8I_8$ crystallizes in the cubic 0D $Cs_6Re_6S_8I_8$ structure type with the space group $Fm\bar{3}m$ (Table 1) containing Rb^+, I^- and $[Re_6S_8I_6]^{4-}$ ions (Fig. 1). The composition was confirmed using energy-dispersive spectroscopy in a scanning electron microscope (SEM) (Supplementary Fig. 4). $Rb_6Re_6S_8I_8$ is the dimensionally reduced 0D rubidium derivative of the three-dimensional parent compound $Re_6S_8I_2$[13]. The 20-atom $[Re_6S_8I_6]^{4-}$ cluster (Fig. 1b) contains a $[Re_6S_8]^{2+}$ cluster core with six rhenium (III) atoms forming an octahedral arrangement with a Re–Re bond length of 2.5950(5) Å. Each sulfur atom caps one face of the octahedron in a μ_3 interaction with three rhenium atoms, resulting in Re–S bond lengths of 2.4043(15) Å. The iodine atoms bound to the cluster exhibit a Re–I bond length of 2.7709(8) Å. This structure type is a derivative of the rock-salt structure. Every $[Re_6S_8]^{2+}$ cluster core replaces one rubidium atom and results in a vacancy at a second rubidium site. The iodine atom bound to the cluster is slightly off the typical iodide position filling space in the vacant rubidium positions due to the bulkier nature of the cluster. Four Rb^+ cations charge balance each $[Re_6S_8I_6]^{4-}$ cluster and are co-crystallized with two additional equivalents of RbI that occupy the remaining sites in the rock-salt arrangement. Of the three inorganic 0D rhenium chalcohalide structure types ($Cs_4Re_6S_8Br_6$ exhibiting no co-crystallized salt, $Cs_5Re_6S_8Cl_7$ exhibiting one equivalent of co-crystallized salt), only compositions containing both sulfur and iodine like $Rb_6Re_6S_8I_8$ co-crystallize with two equivalents of salt in a rock salt arrangement[17,35,37,38].

Electronic and optical properties

The calculated electronic band structure and partial density of states of $Rb_6Re_6S_8I_8$ are presented in Supplementary Fig. 5. $Rb_6Re_6S_8I_8$ is an indirect-band-gap semiconductor, with the conduction-band minimum (CBM) at the X and L points and the valence-band maximum (VBM) along the Γ–K direction (Σ line). The valence band is predominantly flat, while the conduction band shows minimal dispersion (~0.1 eV), consistent with the 0D ionic structure. The partial density of states reveals that Re 4*d* orbitals contribute substantially to the band edges, along with some S 3*p* and Re 5*p* orbitals. Supplementary Information provides further details on phonon dispersion curves, Raman data and stretching modes of $Rb_6Re_6S_8I_8$ (Supplementary Figs. 6–8, respectively).

The optical properties of $Rb_6Re_6S_8I_8$ crystals grown and mechanically separated (Fig. 2) were probed using UV–Vis diffuse reflectance spectroscopy, photoemission yield spectroscopy in air and PL measurements. The band gap (Fig. 2a) was determined to be 2.06(5) eV (602 nm). Additionally, the ionization energy (Fig. 2b), which for semiconductors is the energy of the VBM with respect to the vacuum level, was found to be 5.51(3) eV. Considering the band gap in combination with the VBM gives a CBM of 3.45(6) eV. These values allow for optimization of the band alignment of optoelectronic devices, including LEDs, by enabling the selection of carrier transport materials, which minimizes energy barriers.

To probe the emission properties of $Rb_6Re_6S_8I_8$, the PL was measured at both RT and 77 K (Fig. 2c). The RT emission ranges from 1.01 eV to 2.12 eV (1,230 nm to 585 nm), with a peak maximum at 1.50 eV (827 nm), while the emission slightly narrows at 77 K, emitting from 1.01 eV to 1.88 eV (1,230 nm to 659 nm), with a peak maximum slightly redshifted to 1.45 eV (855 nm). The time-resolved PL of $Rb_6Re_6S_8I_8$ was measured at 293 K and 77 K, and both decays fit well to a single-exponential decay with very long lifetimes of 77 μs and 99 μs respectively (Fig. 2d). The

Table 1 | $Rb_6Re_6S_8I_8$ crystallographic data

Formula weight	5,803.40
Temperature	293 K
Wavelength	0.71073 Å
Crystal system	Cubic
Space group	$Fm\bar{3}m$
Unit-cell dimensions	$a=b=c=15.5443(18)$ Å $\alpha=\beta=\gamma=90°$
Volume	3755.9(13) $Å^3$
Density (calculated)	5.132 g cm^{-3}
Independent reflections	468 ($R_{int}=0.0170$)
Completeness to $\theta=25.242°$	99.1%
Goodness of fit	1.267
Final R indices ($I>2\sigma(I)$)	$R_{obs}=0.0182$ $wR_{obs}=0.0438$
R indices (all data)	$R_{all}=0.0192$ $wR_{all}=0.0439$
Extinction coefficient	0.000271(12)
Largest diff. peak and hole	1.267 and −1.070 e $Å^{-3}$

$R=\sum||F_o|-|F_c||/\sum|F_o|$, $wR=(\sum[w(|F_o|^2-|F_c|^2)^2]/\sum[w(|F_o|^4)])^{1/2}$ and $w=1/[\sigma^2(F_o^2)+(0.0144P)^2+75.2596P]$ where F_o and F_c are observed and calculated structure factor amplitudes respectively and $P=(F_o^2+2F_c^2)/3$.

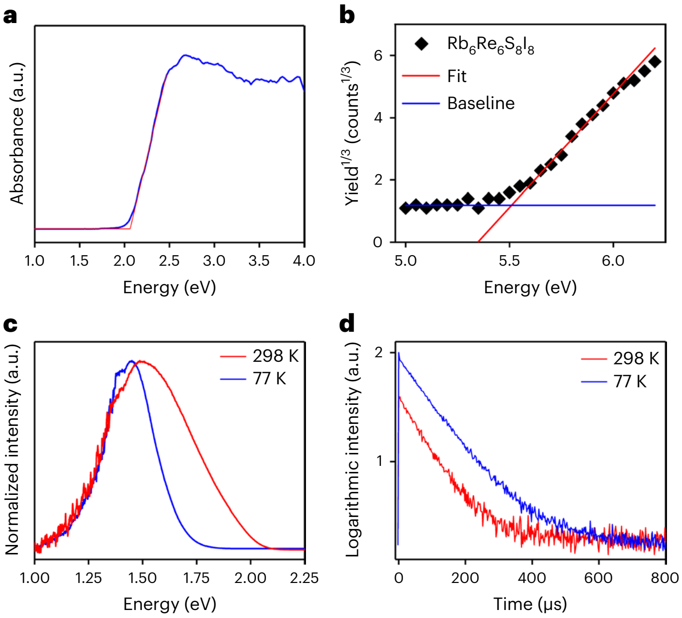

Fig. 2 | $Rb_6Re_6S_8I_8$ optical properties. a, Absorption spectrum of $Rb_6Re_6S_8I_8$ obtained by the Kubelka–Munk transformation of diffuse reflectance data with an absorption edge of 2.06(5) eV. **b**, Ionization energy of $Rb_6Re_6S_8I_8$ with the value of 5.51(3) eV. **c**, Normalized PL at both 298 K and 77 K. The PL maximum shifts from 1.50 eV (827 nm) to 1.45 eV (855 nm), and the maximum emission energy shifts from 2.12 eV (584 nm) to 1.88 eV (659 nm). **d**, Logarithmic-scale plot of the PL lifetime at both 298 K of 77 μs and 77 K of 99 μs.

RT PLQY of $Rb_6Re_6S_8I_8$ crystals is 42.7%. This value is a slight undercount because instrumental limitations only enabled reliable photon counting up to 950 nm (above 1.305 eV). To the best of our knowledge, the highest previously reported PLQY value for any material in this family of cluster compounds or cluster derivative in solution is 23.8% for $[Re_6Se_8(Me_2SO)_6]^{2+}$ with a PL lifetime of 22.4 μs measured in dimethyl sulfoxide solution[10,11].

The origin of the PL for $[Re_6Q_8X_6]^{4-}$ including the $[Re_6S_8I_6]^{4-}$ cluster in $Rb_6Re_6S_8I_8$ has been previously investigated and arises from the contributions of four different triplet states in the cluster[10–12]. Energy differences between the four triplet states are responsible for the PL emission width, while the spin-forbidden relaxations of triplet states explain the long lifetimes of these clusters and how $Rb_6Re_6S_8I_8$ as an indirect-gap semiconductor with fairly flat band edges can have such strong PL[10–12]. The solid-state PL behaviour of the series of tetra-n-butylammonium (n-Bu_4N) salt derivatives, $(n\text{-}Bu_4N)_4Re_6S_8X_6$ (X = Cl, Br, I) was studied by Kitamura et al.[12], including the study of $(n\text{-}Bu_4N)_4Re_6S_8I_6$ salt, which contains the same $[Re_6S_8I_6]^{4-}$ cluster as found in $Rb_6Re_6S_8I_8$. The RT PL emission for $(n\text{-}Bu_4N)_4Re_6S_8I_6$ has a maximum at 1.55 eV (800 nm) with emission up to 2.08 eV (596 nm), which narrows upon cooling to 70 K, emitting only out to 1.80 eV (689 nm), which is similar to what we observe for $Rb_6Re_6S_8I_8$. Interestingly, the 293 K PL lifetime and PLQY of solid $Rb_6Re_6S_8I_8$ are much longer and larger than those reported for $(n\text{-}Bu_4N)_4Re_6S_8I_6$ both in solid state and solubilized in deoxygenated dichloromethane (CH_2Cl_2). The 293 K PL lifetime for $Rb_6Re_6S_8I_8$ of 77 μs is about 30 times longer than that of $(n\text{-}Bu_4N)_4Re_6S_8I_6$, 2.51 μs (2.6 μs when solubilized)[10–12]. Additionally, the 293 K PLQY for $Rb_6Re_6S_8I_8$ of 42.7% is almost 40 times larger than that for $(n\text{-}Bu_4N)_4Re_6S_8I_6$, 0.3% (1.1% when solubilized)[10,11]. As the $[Re_6S_8I_6]^{4-}$ cluster is responsible for the emission in both cases, this difference in lifetime and PLQY seems to arise from the influence of the co-crystallized ions. The n-Bu_4N^+ cations are bulkier than the Rb^+ and I^- ions, resulting in larger cluster distances when compared with $Rb_6Re_6S_8I_8$, where the six nearest-neighbouring $[Re_6S_8I_6]^{4-}$ clusters have a closest distance of ~5 Å. Additionally, it is possible that the numerous vibrational states of the organic n-Bu_4N^+ cation could facilitate non-radiative recombination of electron–hole carriers. Ultimately, these structural differences combine to reduce the interactions causing carrier relaxation via non-radiative pathways, resulting in the impressive optical properties of $Rb_6Re_6S_8I_8$ when compared with $(n\text{-}Bu_4N)_4Re_6S_8I_6$.

Solubility and cluster emission in solution

$Rb_6Re_6S_8I_8$ is soluble in multiple polar solvents (Supplementary Table 6), generally resulting in coloured solutions of pale yellow colour, which darken to orange and then dark orange as the concentration increases. The PL excitation was measured by dissolving phase-pure $Rb_6Re_6S_8I_8$ (Supplementary Fig. 9) in water (Supplementary Fig. 10), exhibiting characteristic emission for the solvated $[Re_6S_8I_6]^{4-}$ cluster with an emission maximum at 1.74 eV (713 nm), which is at slightly higher energy than the emission seen for solid $Rb_6Re_6S_8I_8$.

Solution-processable films

Solution-processed $Rb_6Re_6S_8I_8$ films were fabricated both in air and in a nitrogen glovebox using 0.2 mg $μl^{-1}$ $Rb_6Re_6S_8I_8$ solutions in DMF via one-step spin coating followed by a 30 min anneal at 150 °C, with additional details in Methods. For films cast in air the PXRD of a typical film (Fig. 3a) shows all that the observed reflections match the calculated peak positions for $Rb_6Re_6S_8I_8$. The weak and broad feature in the PXRD between ~15° and ~40° 2θ results from amorphous diffraction from the glass substrate and any amorphous region of the $Rb_6Re_6S_8I_8$ film. The texture of the film was elucidated by grazing-incidence wide-angle scattering. The patterns (Supplementary Fig. 11) are mainly composed of diffraction rings, indicating that many grains are randomly oriented. That said, integrating the (002) and (111) peaks over the angular coordinate χ shows a small population with the (002) peak (Supplementary Fig. 12a) parallel to the substrate, with a larger substantial population of grains oriented with the (111) peak (Supplementary Fig. 12b) parallel to the substrate. A full texture analysis is in the caption for Supplementary Fig. 11. Profilometry measurements of a typical film cast in air (Supplementary Fig. 13a) find an average thickness of 152.7 nm and a roughness of 15.0 nm. SEM images (Supplementary Fig. 14a) indicate

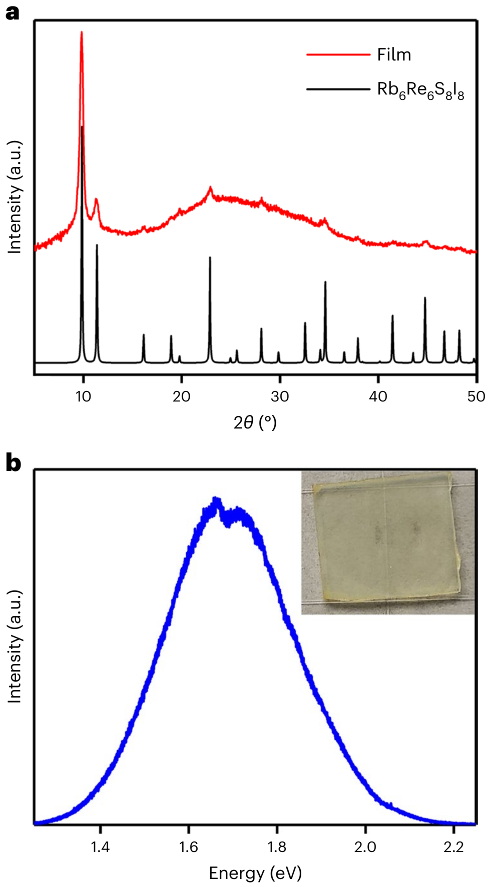

Fig. 3 | $Rb_6Re_6S_8I_8$ thin films. a, PXRD of a $Rb_6Re_6S_8I_8$ film indicating phase purity. **b**, PL from a $Rb_6Re_6S_8I_8$ film showing retention of the PL emission range when cast as a film. Inset: image of a $Rb_6Re_6S_8I_8$ thin film deposited on a glass substrate.

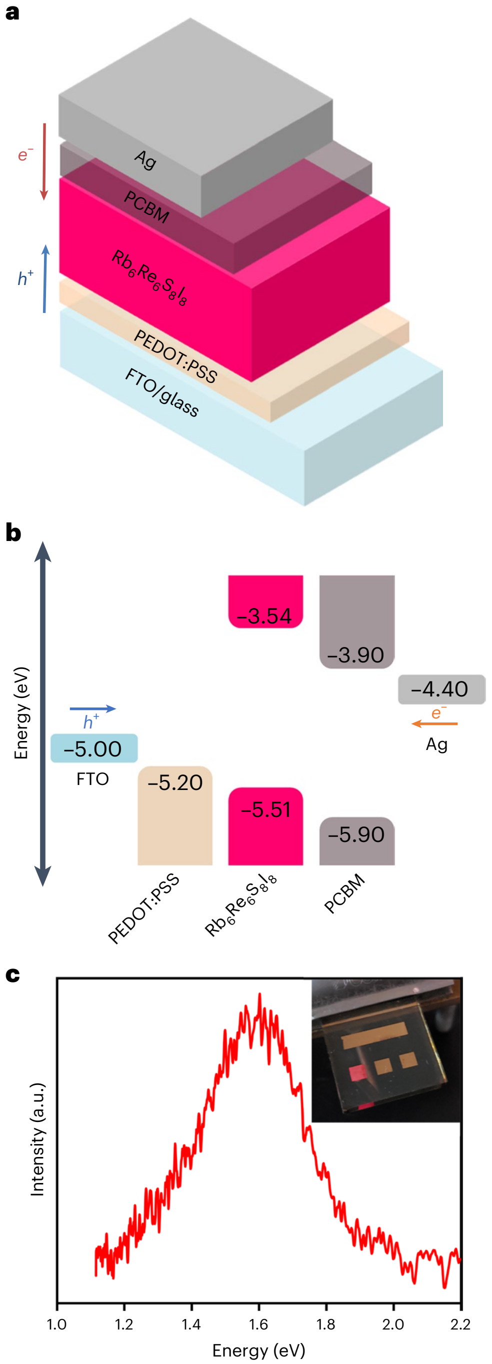

Fig. 4 | Initial $Rb_6Re_6S_8I_8$ LED performance. a–c, Device architecture (**a**), band alignment diagram (**b**) and emission spectra (**c**) of an LED. Inset: a device turned on.

that the surfaces of films prepared in air exhibit a matrix of material with small cube-shaped crystallites (~100 nm to 1 µm) both embedded and on the surface of the film, in addition to needle-like features. The film retains the same PL emission range, with the emission maximum slightly blueshifted to 1.68 eV (738 nm) (Fig. 3b) when compared with the bulk $Rb_6Re_6S_8I_8$ emission. This small shift may arise due to a confinement effect from the small crystallites (<1 µm) in the film. The PL lifetime (Supplementary Fig. 15) required a two-component exponential decay fit with reduced PL lifetimes when compared with the bulk unprocessed material. The first component lifetime is 8.75 µs and the second is 30.4 µs, for a weighted-average PL lifetime of 22.5 µs for a $Rb_6Re_6S_8I_8$ film, probably due to a combination of strain, defects and reduced crystallinity when compared with the bulk.

Films cast in a nitrogen glovebox exhibit weaker PXRD diffraction intensity (Supplementary Fig. 16a), attributed to the fact that they are nearly three times thinner than those cast in air. However, observable reflections confirm phase purity, while the PL range is slightly narrower, emitting up to 2.00 eV (620 nm) instead of 2.15 eV (577 nm) (Supplementary Fig. 16b). Profilometry measurements show an average thickness of 59.5 nm and a roughness of 16.7 nm (Supplementary Fig. 13b). SEM images reveal a continuous matrix film with small cube-shaped crystallites (~100 nm to 1 µm) both embedded and on the surface, lacking the needle-like features seen in air-cast films (Supplementary Fig. 14b). Further analysis of films deposited on indium tin oxide (ITO)/PEDOT:PSS is available in Supplementary Information (Supplementary Fig. 17).

Antisolvent[39] and hot casting[40] were explored to improve the quality of film cast in a nitrogen glovebox. For the antisolvent treatment two fresh films were prepared and one was treated with chlorobenzene as the antisolvent. SEM images (Supplementary Fig. 18) revealed smoother film surfaces with reduced surface features in the antisolvent-treated film. PXRD analysis (Supplementary Fig. 19a) showed increased crystallinity, indicated by higher intensity for the first two reflections, which are the (111) and the (200) peaks in the diffraction pattern. However, this increase was accompanied by a slight decrease in PL intensity (Supplementary Fig. 19b). For hot casting two fresh films were prepared, with one substrate preheated to 150 °C. The film prepared using hot casting exhibited approximately four times higher PL intensity (Supplementary Fig. 20a). SEM images (Supplementary Fig. 20b) showed a rougher surface texture, with thin lines separating crystallites of approximately 1 µm^2 in area.

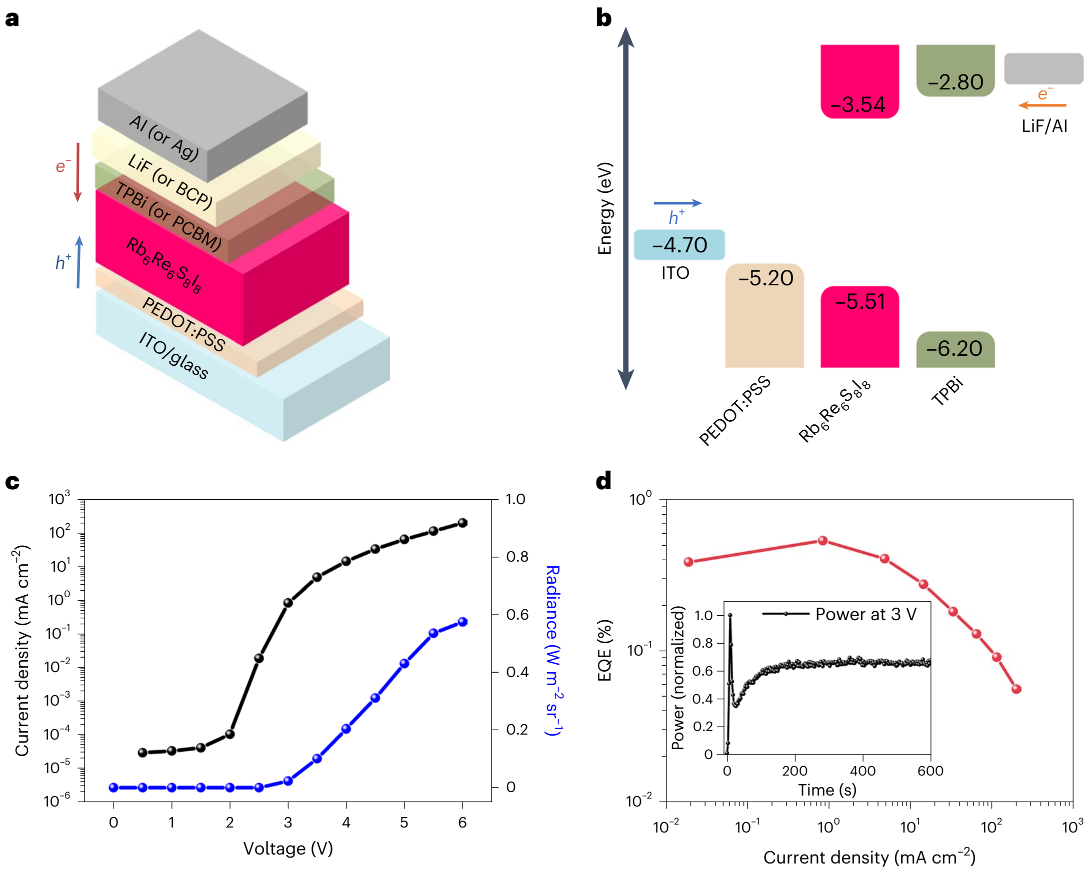

Fig. 5 | Optimized $Rb_6Re_6S_8I_8$ LED performance. a, Updated device architecture with either the addition of the BCP layer or the use of TPBi as the electron transport layer with LiF/Al as electrode layers. **b**, Band alignment diagram of the TPBi/LiF/Al device architecture. **c**, *J*–*V* curve and radiance data for the TPBi device architecture. This architecture exhibits a lower leakage current and higher shunt resistance than the PCBM/BCP/Ag architecture. **d**, The EQE of the device as a function of current density shows that a maximum EQE of 0.535% was achieved. Inset: stability test measuring the time-dependent power of a device that includes the BCP layer held at a constant applied bias of 3 V.

Light-emitting devices

Solution-processed thin films of $Rb_6Re_6S_8I_8$ were incorporated as the active layer of LEDs, demonstrating the potential for rhenium chalcohalide clusters as a solution-processable thin-film material in optoelectronic devices. The device architecture and band alignment diagram of the initially constructed LED device (Fig. 4a,b) uses fluorine-doped tin oxide (FTO) as a transparent contact, PEDOT:PSS as a hole transport layer, $Rb_6Re_6S_8I_8$ as the active material, [6,6]-phenyl-C_{61}-butyric acid methyl ester (PCBM) as the electron transport layer and silver as the second electrical contact. The emission spectrum of the device (Fig. 4c) was measured under a constant bias of 3 V (an image of the functioning device is shown in the inset). The device emission ranges from 1.20 eV (1,030 nm) to 1.85 eV (670 nm) with a maximum at 1.60 eV (775 nm), consistent with the behaviour of the bulk material. Increasing the applied bias to 4 V or more resulted in device failure. When the voltage was kept to 3.5 V or lower, the device could be powered off and back on again. Examination of the current-density (*J*)–voltage (*V*) data (Supplementary Fig. 21) shows diode rectifying *J*–*V* behaviour for the device, with a typical turn-on voltage of 2.1 V. The use of a bathocuproine (BCP) layer in between the PCBM and Ag layers is known to improve solar-cell device performance by alleviating charge buildup at the interfaces and reducing the barrier-to-carrier flow in devices[41]. On the basis of this approach, we tested a similar device architecture (Fig. 5a) that includes a BCP layer. Additionally, the transparent contact was switched to ITO and both hot-casting and antisolvent methods were used in the $Rb_6Re_6S_8I_8$ film fabrication steps. A comparison of the *J*–*V* curve data (Supplementary Fig. 21) demonstrates that the inclusion of a BCP layer in the device architecture maintained diode rectifying behaviour while decreasing the turn-on voltage to 1.7 V. Time-dependent device stability tests were performed, monitoring the power (W) of a device with a constant voltage of 3 V as a function of time after turning on a device. The device initially stabilized its power consumption after 100 s and no power output loss occurred during the next 500 s (inset of Fig. 5d).

In an effort to improve the device efficiency, a second architecture was tested (Fig. 5a), exhibiting a band alignment with reduced electron injection energy barrier (Fig. 5b). The ITO/PEDOT:PSS/$Rb_6Re_6S_8I_8$ was unchanged while the electron transport layer was changed to 1,3,5-tris(1-phenyl-1H-benzimidazol-2-yl)-benzene (TPBi) with a LiF and then Al layer used as the other electrical contact[42]. A comparison of the *J*–*V* data for the PCBM/BCP/Ag and TPBi/LiF/Al architectures (Supplementary Fig. 22) indicates that both show diode rectifying *J*–*V* behaviour while the TPBi/LiF/Al architecture has a lower leakage current, higher shunt resistance and similar turn-on voltage to the PCBM/BCP/Ag architecture. Voltage-dependent radiance measurements and external quantum efficiency (EQE) measurements (Fig. 5c,d) were carried out for the TPBi/LiF/Al architecture, and a maximum EQE of 0.535% was achieved.

Outlook

$Rb_6Re_6S_8I_8$ is a new solution-processable 0D rhenium chalcohalide material containing isolated $[Re_6S_8I_6]^{4-}$ clusters crystallizing in the space group $Fm\bar{3}m$. It exhibits broad RT PL in the red to near-IR region with a PLQY of 42.7% and a PL lifetime of 77 µs (99 µs at 77 K). The 0D structure enables solubility in polar solvents including DMF, allowing for solution processing of the material into photoluminescent thin films. Thin films of $Rb_6Re_6S_8I_8$ were then incorporated as the active layer into a functioning proof-of-concept LED, demonstrating the potential for rhenium chalcohalides as solution-processable optically active films in optoelectronic devices.

Online content

Any methods, additional references, Nature Portfolio reporting summaries, source data, extended data, supplementary information, acknowledgements, peer review information; details of author contributions and competing interests; and statements of data and code availability are available at https://doi.org/10.1038/s41563-023-01740-9.

References

1. Chung, I., Lee, B., He, J. Q., Chang, R. P. H. & Kanatzidis, M. G. All-solid-state dye-sensitized solar cells with high efficiency. *Nature* **485**, 486–489 (2012).
2. Lee, M. M., Teuscher, J., Miyasaka, T., Murakami, T. N. & Snaith, H. J. Efficient hybrid solar cells based on meso-superstructured organometal halide perovskites. *Science* **338**, 643–647 (2012).
3. Tsai, H. H. et al. High-efficiency two-dimensional Ruddlesden–Popper perovskite solar cells. *Nature* **536**, 312–316 (2016).
4. Lin, K. B. et al. Perovskite light-emitting diodes with external quantum efficiency exceeding 20 per cent. *Nature* **562**, 245–248 (2018).
5. Xiao, Z. G. et al. Efficient perovskite light-emitting diodes featuring nanometre-sized crystallites. *Nat. Photon.* **11**, 108–115 (2017).
6. Ghorpade, U. V. et al. Emerging chalcohalide materials for energy applications. *Chem. Rev.* **123**, 327–378 (2023).
7. Roth, A. N. et al. Solution-phase synthesis and photoluminescence of quaternary chalcohalide semiconductors. *Chem. Mater.* **35**, 2165–2172 (2023).
8. Xiao, J.-R., Yang, S.-H., Feng, F., Xue, H.-G. & Guo, S.-P. A review of the structural chemistry and physical properties of metal chalcogenide halides. *Coord. Chem. Rev.* **347**, 23–47 (2017).
9. Islam, S. M. et al. Direct gap semiconductors $Pb_2BiS_2I_3$, $Sn_2BiS_2I_3$, and Sn_2BiSI_5. *Chem. Mater.* **28**, 7332–7343 (2016).
10. Gray, T. G., Rudzinski, C. M., Nocera, D. G. & Holm, R. H. Highly emissive hexanuclear rhenium(III) clusters containing the cubic cores $[Re_6S_8]^{2+}$ and $[Re_6Se_8]^{2+}$. *Inorg. Chem.* **38**, 5932–5933 (1999).
11. Gray, T. G., Rudzinski, C. M., Meyer, E. E., Holm, R. H. & Nocera, D. G. Spectroscopic and photophysical properties of hexanuclear rhenium(III) chalcogenide clusters. *J. Am. Chem. Soc.* **125**, 4755–4770 (2003).
12. Kitamura, N. et al. Temperature dependent emission of hexarhenium(III) clusters $[Re_6(\mu_3\text{-}S)_8X_6]^{4-}$ ($X = Cl^-$, Br^-, and I^-): analysis by four excited triplet-state sublevels. *Inorg. Chem.* **44**, 6308–6313 (2005).
13. Laing, C. C. et al. Photoluminescent $Re_6Q_8I_2$ (Q=S, Se) semi-conducting cluster compounds. *Chem. Mater.* **33**, 5780–5789 (2021).
14. Opalovskii, A. A., Fedorov, V. E. & Lobkov, E. U. The reaction of molybdenum, tungsten, and rhenium selenides with gaseous bromine. *Russ. J. Inorg. Chem.* **16**, 790–792 (1971).
15. Opalovskii, A. A., Fedorov, V. E., Lobkov, E. U. & Erenburg, B. G. New rhenium chalcogenide halides. *Russ. J. Inorg. Chem.* **16**, 1685 (1971).
16. Batail, P., Ouahab, L., Pénicaud, A., Lenoir, C. & Perrin, A. Preparation of the tetrabutylammonium salt of a rhenium (III) chalcohalide molecular cluster, $(C_4H_9)_4NRe_6Se_5Cl_9$. Access to the solution-phase chemistry of an analogous molybdenum chalcogenide, examples of electrochemical association with tetrathia(selena)fulvalene-based cationic radicals. *C. R. Acad. Sci. II* **304**, 1111–1116 (1987).
17. Long, J. R., Williamson, A. S. & Holm, R. H. Dimensional reduction of $Re_6Se_8Cl_2$: sheets, chains, and discrete clusters composed of chloride-terminated $[Re_6Q_8]^{2+}$ (Q=S, Se) cores. *Angew. Chem. Int. Ed. Engl.* **34**, 226–229 (1995).
18. Willer, M. W., Long, J. R., McLauchlan, C. C. & Holm, R. H. Ligand substitution reactions of $[Re_6S_8Br_6]^{4-}$: a basis set of Re_6S_8 clusters for building multicluster assemblies. *Inorg. Chem.* **37**, 328–333 (1998).
19. Selby, H. D., Roland, B. K. & Zheng, Z. Ligand-bridged oligomeric and supramolecular arrays of the hexanuclear rhenium selenide clusters—exploratory synthesis, structural characterization, and property investigation. *Acc. Chem. Res.* **36**, 933–944 (2003).
20. Shestopalov, M. A. et al. Self-assembly of ambivalent organic/inorganic building blocks containing Re_6 metal atom cluster: formation of a luminescent honeycomb, hollow, tubular metal–organic framework. *Inorg. Chem.* **48**, 1482–1489 (2009).
21. Pinkard, A., Champsaur, A. M. & Roy, X. Molecular clusters: nanoscale building blocks for solid-state materials. *Acc. Chem. Res.* **51**, 919–929 (2018).
22. Satoshi, K., Sayoko, N. & Teiji, C. Catalytic hydrogenation and dehydrogenation over solid-state rhenium sulfide clusters with an octahedral metal framework. *Chem. Lett.* **36**, 1340–1341 (2007).
23. Kim, Y., Fedorov, V. E. & Kim, S.-J. Novel compounds based on $[Re_6Q_8(L)_6]^{4-}$ (Q=S, Se, Te; L=CN, OH) and their applications. *J. Mater. Chem.* **19**, 7178–7190 (2009).
24. Kubeil, M. et al. Sugar-decorated dendritic nanocarriers: encapsulation and release of the octahedral rhenium cluster complex $[Re_6S_8(OH)_6]^{4-}$. *Chem. Asian J.* **5**, 2507–2514 (2010).
25. Bruck, A. M. et al. Reversible electrochemical lithium-ion insertion into the rhenium cluster chalcogenide–halide $Re_6Se_8Cl_2$. *Inorg. Chem.* **57**, 4812–4815 (2018).
26. Choi, B. et al. Two-dimensional hierarchical semiconductor with addressable surfaces. *J. Am. Chem. Soc.* **140**, 9369–9373 (2018).
27. Zhong, X. et al. Superatomic two-dimensional semiconductor. *Nano Lett.* **18**, 1483–1488 (2018).
28. He, S. et al. Site-selective surface modification of 2D superatomic Re_6Se_8. *J. Am. Chem. Soc.* **144**, 74–79 (2022).
29. Gabriel, J.-C. P., Boubekeur, K., Uriel, S. & Batail, P. Chemistry of hexanuclear rhenium chalcohalide clusters. *Chem. Rev.* **101**, 2037–2066 (2001).
30. Fischer, C. et al. Structure and photoelectrochemical properties of semiconducting rhenium cluster chalcogenides: $Re_6X_8Br_2$ (X=S, Se). *J. Alloys Compd.* **178**, 305–314 (1992).
31. Fischer, C., Fiechter, S., Tributsch, H., Reck, G. & Schultz, B. Crystal structure and thermodynamic analysis of the new semiconducting Chevrel phase $Re_6S_8Cl_2$. *Ber. Bunsenges. Phys. Chem.* **96**, 1652–1658 (1992).
32. Speziali, N. L. et al. Single crystal growth, structure and characterization of the octahedral cluster compound $Re_6Se_8Br_2$. *Mater. Res. Bull.* **23**, 1597–1604 (1988).
33. Leduc, L., Perrin, A. & Sergent, M. Structure du dichlorure et octaseleniure d'hexarhenium, $Re_6Se_8Cl_2$: compose bidimensionnel a clusters octaedriques Re_6. *Acta Crystallogr. C* **39**, 1503–1506 (1983).
34. Pilet, G., Hernandez, O. & Perrin, A. Crystal structure of rhenium caesium sulfobromide, $CsRe_6S_8Br_3$, the first cluster compound in the Cs–Re–S–Br system exhibiting two types of inter-unit bridges. *Z. Kristallogr. New Cryst. Struct.* **217**, 11–12 (2002).
35. Pilet, G. & Perrin, A. New compounds in the cesium sulfobromide rhenium octahedral cluster chemistry: syntheses and crystal structures of $Cs_4Re_6S_8Br_6$ and $Cs_2Re_6S_8Br_4$. *Solid State Sci.* **6**, 109–116 (2004).
36. Yarovoi, S. S., Mironov, Y. V., Tkachev, S. V. & Fedorov, V. E. Phase formation in the Re–Se–Br–MBr systems (M=Li, Na, K, Rb, Cs). *Russ. J. Inorg. Chem.* **54**, 299–304 (2009).

37. Long, J. R., McCarty, L. S. & Holm, R. H. A solid-state route to molecular clusters: access to the solution chemistry of $[Re_6Q_8]^{2+}$ (Q=S, Se) core-containing clusters via dimensional reduction. *J. Am. Chem. Soc.* **118**, 4603–4616 (1996).
38. Solodovnikov, S. F., Yarovoi, S. S., Mironov, Y. V., Vironets, A. V. & Fedorov, V. E. Unusual disordering of potassium ions in the structures of cluster rhenium thiohalides $K_3[Re_6S_7Br_7]$ and $K_4[Re_6S_8Cl_6]$. *J. Struct. Chem.* **45**, 865–873 (2004).
39. Jeon, N. J. et al. Solvent engineering for high-performance inorganic–organic hybrid perovskite solar cells. *Nat. Mater.* **13**, 897–903 (2014).
40. Nie, W. et al. High-efficiency solution-processed perovskite solar cells with millimeter-scale grains. *Science* **347**, 522–525 (2015).
41. Chen, C. et al. Effect of BCP buffer layer on eliminating charge accumulation for high performance of inverted perovskite solar cells. *RSC Adv.* **7**, 35819–35826 (2017).
42. Kim, N. et al. Highly efficient vacuum-evaporated $CsPbBr_3$ perovskite light-emitting diodes with an electrical conductivity enhanced polymer-assisted passivation layer. *ACS Appl. Mater. Interfaces* **13**, 37323–37330 (2021).

Publisher's note Springer Nature remains neutral with regard to jurisdictional claims in published maps and institutional affiliations.

Springer Nature or its licensor (e.g. a society or other partner) holds exclusive rights to this article under a publishing agreement with the author(s) or other rightsholder(s); author self-archiving of the accepted manuscript version of this article is solely governed by the terms of such publishing agreement and applicable law.

© The Author(s), under exclusive licence to Springer Nature Limited 2024

Methods

Reagents

Re (99.997%, ProChem), S (99.99%, 5N Plus) and I_2 (99.8%, Sigma-Aldrich) were used as purchased without additional purification. RbI (99.9%, Alfa Aesar) was melted with a methane and oxygen torch under dynamic vacuum and then allowed to cool and recrystallize before use.

$Rb_6Re_6S_8I_8$ synthesis

$Rb_6Re_6S_8I_8$ was synthesized from RbI (0.9600 g, 4.520 mmol), Re (0.2525 g, 1.356 mmol) and S (0.0580 g, 1.81 mmol) that were mechanically mixed in air in an agate mortar and pestle and then charged to a fused silica tube (15 mm outer diameter and 12 mm inner diameter) lined with Al foil to prevent powder from sticking to the walls. I_2 (0.2295 g, 0.9014 mmol) was then added on top of the mixture and the Al foil was discarded. This resulted in a 20:6:8:4 molar ratio of RbI:Re:S:I_2 in the tube. The tube was then evacuated until a pressure of 1.0×10^{-2} mbar was reached and cooled with liquid nitrogen for 30 s. This condenses the I_2 and prevents it from escaping, while having provided time for water vapour and oxygen to have been removed without condensing in the tube. The tube was then flame-sealed at 3.0×10^{-3} mbar with an internal length of 10 cm. To prevent vapour transport of ReS_2, the sealed tube was positioned in a one-zone tube furnace such that the reagents were adjacent to the thermocouple near the cooler outer edge of the furnace while the other end of the tube is in the hotter centre of the furnace. To prevent overpressurization of the tube, the iodine pressure was estimated assuming all of the iodine was a gas at the maximum temperature with 36% dissociation[43] for a maximum calculated pressure of 9.5 atm. The furnace was heated to 800 °C over 9 h, held there for 36 h, cooled to 625 °C at a rate of 2 °C h^{-1} and then turned off and allowed to cool to RT. Orange crystals of $Rb_6Re_6S_8I_8$ suitable for characterization were mechanically separated from the rest of the product. The procedure for the synthesis and recrystallization of larger quantities $Rb_6Re_6S_8I_8$ is discussed in Supplementary Information along with PXRD demonstrating phase purity (Supplementary Fig. 23) and images of $Rb_6Re_6S_8I_8$ powder exhibiting PL under UV light (Supplementary Fig. 24).

$Rb_6Re_6S_8I_8$ film fabrication

Films of $Rb_6Re_6S_8I_8$ were made both in air and in a nitrogen glovebox by spin coating solutions of $Rb_6Re_6S_8I_8$ onto a cleaned glass substrate. The glass substrates were cleaned by sequentially submerging and sonicating the substrates for 5 min each in aqueous detergent, deionized water, acetone and then ethanol, followed by a 5 min UV–ozone treatment. The $Rb_6Re_6S_8I_8$ solutions were prepared at a concentration of 0.2 mg μl^{-1} using recrystallized phase-pure $Rb_6Re_6S_8I_8$, prepared as described in Supplementary Information, and anhydrous DMF in a glovebox. The solution was allowed to sit at ambient temperature for an hour until no visible solid remained, at which point the solution was syringe filtered with a 0.2 µm disposable polytetrafluoroethylene filter. Then 50 µl of $Rb_6Re_6S_8I_8$ solution was deposited on the cleaned glass substrate and spread to cover the entire substrate. The spin coating was carried out at 4,000 r.p.m. for 30 s. This was followed by 30 min of annealing at 150 °C on a hot plate. The films have a yellow/orange tint. For the hot-casting method, the substrate was preheated at 150 °C for 5 min before the $Rb_6Re_6S_8I_8$ solution-coating process. For the antisolvent method, 200 µl of chlorobenzene was poured 25 s after starting the $Rb_6Re_6S_8I_8$ solution-coating process.

LED fabrication

FTO and ITO substrates were cleaned by sequentially submerging and sonicating the substrates for 5 min each in aqueous detergent, deionized water, acetone and then ethanol, followed by a 20 min UV treatment. PEDOT:PSS solution (50 µl) was used as the hole transport layer by spin coating at 6,000 rpm for 30 s followed by a 30 min annealing at 150 °C in air. At this point the substrate was transferred to a glovebox for the rest of the device fabrication process. 50 µl of $Rb_6Re_6S_8I_8$ in anhydrous DMF solution (0.252 mg μl^{-1} concentration prepared in an manner otherwise identical to that described in the film fabrication section) was spin coated at 4,000 r.p.m. for 30 s followed by a 150 °C annealing step for 30 min. A layer of PCBM as the electron transport layer (30 µl of a 0.02 mg μl^{-1} solution in chlorobenzene) was spin coated at 1,000 r.p.m. for 60 s without an annealing step. This was then followed by thermal deposition in a metal deposition chamber of silver to make a 100-nm-thick layer.

Devices were also constructed that included a BCP layer (5 nm) between the PCBM and Ag layers. BCP (0.001 mg μl^{-1} solution in iso-propanol) was spin coated at 5,000 rpm for 30 s without an annealing step. Devices prepared this way used ITO instead of FTO as the transparent electrode in addition to a modification to the $Rb_6Re_6S_8I_8$ film fabrication step. 200 µl of chlorobenzene as an antisolvent was poured 25 s after starting the $Rb_6Re_6S_8I_8$ solution coating process and the substrate was preheated at 150 °C for 5 min before the $Rb_6Re_6S_8I_8$ solution coating process.

Devices were also constructed using TPBi/LiF/Al instead of the PCBM/BCP/Ag layers for the electron transport layer side of the device. The modified procedure for $Rb_6Re_6S_8I_8$ films was used for these devices. Thermal evaporation was used to deposit a 50-nm-thick layer of TPBi under a high vacuum ($<10^{-6}$ torr). The LiF and Al electrode layers (1 nm/100 nm thickness) were also deposited by thermal evaporation under high vacuum. The LEDs constructed had one of three areas: 0.05 cm^2, 0.09 cm^2 or 0.39 cm^2.

Single-crystal X-ray diffraction

Intensity data were collected from a suitable irregularly shaped crystal of $Rb_6Re_6S_8I_8$ mounted on a glass fibre with superglue and diffracted using an IPDS 2 single-crystal X-ray diffractometer at 293 K operating at 50 kV and 40 mA with Mo Kα radiation ($\lambda = 0.71073$ Å), a sealed X-ray source with X-ray fibre optics and an image plate detector. Data collection, data reduction and a numerical absorption correction were performed using the STOE X-Area v.1.90 software package, STOE X-Red v.1.65.2 and STOE X-Shape v.2.21[44] followed by scaling and outlier rejection with STOE LANA v.1.83.8[45]. The structure solution was performed using the SHELXT intrinsic phasing solution method[46] and was refined with the SHELXL full-matrix least-squares minimization of F^2 method[47]. OLEX2[48] v.1.5 was used as the graphical interface. Select crystallographic information can be found in Table 1 and complete crystallographic information can be found in Supplementary Tables 1–5.

Data availability

All data supporting the findings are provided as figures and accompanying tables in the article and Supplementary Information. The X-ray crystallographic coordinates for the structure reported in this study have been deposited at the Cambridge Crystallographic Data Centre (CCDC) with deposit number 2241320. These data can be obtained free of charge from the CCDC via www.ccdc.cam.ac.uk/data_request/cif. Data files for all figures are available from the corresponding author upon reasonable request.

Code availability

The custom codes used in this work are available upon reasonable request.

References

43. DeVries, T. & Rodebush, W. H. The thermal dissociation of iodine and bromine. *J. Am. Chem. Soc.* **49**, 656–666 (1927).
44. X-Area v.1.90, X-Red v.1.65.2, X-Shape v.2.21 (STOE, 2020).
45. Koziskova, J., Hahn, F., Richter, J. & Kožíšek, J. Comparison of different absorption corrections on the model structure of tetra kis(μ-acetato)-diaqua-di-copper(II). *Acta Chim. Slov.* **9**, 136–140 (2016).

46. Sheldrick, G. SHELXT—integrated space-group and crystal-structure determination. *Acta Crystallogr. A* **71**, 3–8 (2015).
47. Sheldrick, G. Crystal structure refinement with SHELXL. *Acta Crystallogr. C* **71**, 3–8 (2015).
48. Dolomanov, O. V., Bourhis, L. J., Gildea, R. J., Howard, J. A. K. & Puschmann, H. OLEX2: a complete structure solution, refinement and analysis program. *J. Appl. Crystallogr.* **42**, 339–341 (2009).

Acknowledgements

This work is supported in part by the National Science Foundation through the MRSEC program (NSF-DMR 1720139) at the Materials Research Center and in part through DMR-2305731. The work made use of the IMSERC Physical Characterization facility at Northwestern University, which has received support from the Soft and Hybrid Nanotechnology Experimental (SHyNE) Resource (NSF ECCS-2025633) and from Northwestern University. It also made use of the EPIC and Keck-II facilities of Northwestern University's NUANCE Center, which have both received support from the SHyNE Resource (NSF ECCS-2025633), the IIN and Northwestern's MRSEC programme (NSF DMR-1720139). The work made use of the GIANTFab core facility at Northwestern University. GIANTFab is supported by the Institute for Sustainability and Energy at Northwestern and the Office of the Vice President for Research at Northwestern. Photoemission yield spectroscopy in air measurements were carried out with equipment acquired using ONR grant N00014-18-1-2102. This research used resources of the Advanced Photon Source Beamline 8-ID-E, a US Department of Energy (DOE) Office of Science User Facility operated for the DOE Office of Science by Argonne National Laboratory under contract DE-AC02-06CH113. We acknowledge M. Quintero, D. Chica and R. McClain for productive conversations.

Author contributions

C.C.L. developed the concept, performed all material synthesis, performed and analysed X-ray crystallography and characterization measurements, and fabricated both thin films and LED devices in addition to their characterization. D.K., J.P. and B.S. fabricated and characterized thin films and LED devices. J.S., J.H. and C.W. performed theoretical and computational work and identified Raman stretching modes. I.H. carried out low-temperature PL measurements and analysis. J.M.H. carried out grazing-incidence wide-angle scattering measurements and assisted in some thin-film and LED device fabrication. C.C.L. and M.G.K. were the primary writers of the paper and the principal investigators. All authors discussed the results and provided feedback on the paper.

Competing interests

The authors declare the patent application PCT/US2023/028799.

Additional information

Supplementary information The online version contains supplementary material available at https://doi.org/10.1038/s41563-023-01740-9.

Correspondence and requests for materials should be addressed to Mercouri G. Kanatzidis.

Peer review information *Nature Materials* thanks Hiroshi Kageyama, Mahesh P. Suryawanshi and the other, anonymous, reviewer(s) for their contribution to the peer review of this work.

Reprints and permissions information is available at www.nature.com/reprints.